Characterization of surface radar cross sections at W-band at moderate incidence angles

Article

Accepted Version

It is advisable to refer to the publisher's version if you intend to cite from the work. See Guidance on citing.

CentAUR

Central Archive at the University of Reading

Reading's research outputs online

Characterization of surface radar cross sections at W-band at moderate incidence angles

Alessandro Battaglia, Mengistu Wolde, Leo Pio D'Adderio, Cuong Nguyen, Franco Fois, Anthony Illingworth, Rolv Midthassel

Abstract—This paper presents the results of a recent flight campaign conducted over the Great Lakes Region and reports the first observations of the W-band normalized backscattered cross section (σ_0) for V and H polarization and the Linear Depolarization Ratios (LDR) from different types of surfaces at moderate incidence angles (<70 degrees).

For sea surfaces, while the observed σ_0 behaves as previously reported at small incidence angles, it features a marked decrease with increasing incidence angles between $20°$ and $50°$. There is a strong dependence of normalized backscattered cross sections both on the wind speed and on the wind direction, with larger values found in the presence of higher wind speeds and when the radar antenna is looking up-wind. This is in line with theoretical models (though models tend to over-predict the range of variability at a given incidence angle) and with observations at lower frequencies. The linear depolarization ratios are steadily increasing from values certainly lower than -30 dB, at vertical incidence, to values of about -10 dB, at incidence angles of about $60°$-$70°$, with a good matching between observations and theoretical predictions.

On the other hand land surface backscattering properties are not characterised by a strong angular dependence: σ_0 and LDR values typically range between -20 and 0 dB and between -15 and -5 dB, respectively.

This study is relevant for space-borne concepts of W-band radars which envisage moderate incidence angles to achieve a broad swath needed for global coverage.

Index Terms—Radar theory, radar surface cross sections, depolarization ratios, W-band

I. INTRODUCTION

Direct observations of the vertical structure of winds are the fundamental observables needed for further advancing numerical weather prediction, [1]. The Aeolus Doppler Wind Lidar satellite mission promises to provide line-of-sight winds in clear air with a clear benefit for data assimilation, [2]. Whilst Doppler-lidar technology is mature, the radar scientific community has been active in the last 5 years in proposing different space-borne Doppler radar system concepts focused at capturing the structure of winds within clouds and precipitating systems. Following previous work based on ground-based observations [3] and space-borne notional studies [4] recent ESA-funded studies have recommended the use of polarization diversity to overcome the range-Doppler dilemma and the short decorrelation times associated with the Doppler fading inherent to millimeter radar systems mounted on fast moving LEO platforms [5]. Two specific applications have been proposed.

1) A conically scanning Dopplerised 94 GHz radar is key to the WIVERN project [6] that aims to provide global in-cloud winds and thus improve forecasts of hazardous weather. To achieve global coverage an 800 or 1700 km swath is envisaged, so it is important to know the vertical extent of surface returns at 40 to $60°$ incidence angle and how these returns will restrict the minimum height above the surface where winds can be derived.

2) A stereoradar configuration for observing the microphysical and dynamical structures of cloud systems, including disturbed mesoscale convective systems, [7].

Such radar configurations adopt different scanning strategies with the commonality of adopting looks at moderate oblique angles (i.e. larger than $40°$ incidence angles). In order to refine such concepts and rigorously assess their potentials there is urgent need to characterize the surface backscattering returns at such slant angles both over water and land surfaces. The signal from the surfaces in fact can alter the atmospheric signal (e.g. corresponding to low clouds or precipitation) mainly via three mechanisms.

1) The surface clutter associated to the antenna mainlobe contaminates the hydrometeor Doppler signal in the lower troposphere, thus reducing the profiling capabilities for ranges close to the surface range. Note that this effect cannot be mitigated via spectral processing like in [8] if polarization diversity pulse pair methodology is adopted for Doppler analysis.

2) The surface clutter associated to antenna sidelobes and range sidelobes -in case pulse compression is adopted-has also detrimental effects both for reflectivities and Doppler moments, [9].

3) Strongly depolarizing surfaces can generate strong and deep "blind layers" high up in the atmosphere when adopting polarization diversity Doppler radars, [4], [5], [7].

While [10] analysed the CloudSat surface return probability distribution function for different surface types and provide a good overview about σ_0 values typically encountered at 94 GHz for nadir incidence, measurements of sea and land surface return at W-band at incidence angles larger than $25°$ are almost not existent at the moment, [11].

Moreover, while at centimeter wavelengths great progress have been done thanks to the availability of a gamut of scatterometer data, at millimeter-wavelenghts the ocean surface backscattering mechanism is still not well understood, in part, due to the lack of experimental measurements. The mechanisms responsible for microwave ocean scattering at low incidence angles ($< 20°$) are different from those at mid incidence angles. Bragg scattering is the major contributor at mid incidence angles. At low incidence, close to nadir, the
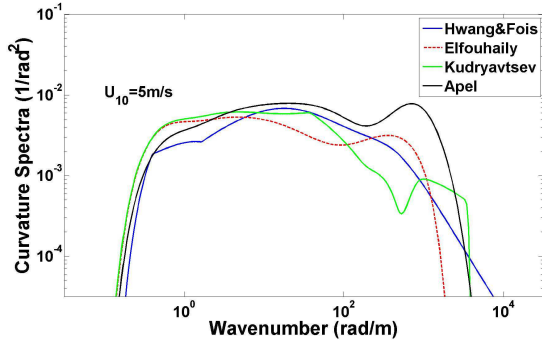
Fig. 1: Comparison of omni-directional curvature spectra for a wind speed of 5 m/s at 10 m altitude.
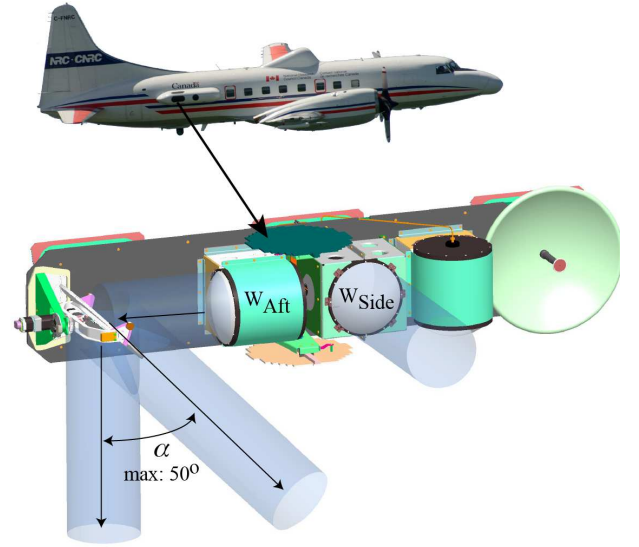

Fig. 2: The NRC Convair-580 Airborne W and X-band (NAWX) radar installation inside a blister radome. In this paper the W-band fixed dual-pol side-looking antennas and the Aft-looking antenna with a two-axis reflector are used. The schematic aft antenna beam redirected to nadir and up to $50°$ forward along the flight direction.

scattering is dominated by the geometric optics and physical optics mechanisms. In this region, a quasi-specular scattering model is often used to describe the radar cross-section [12]. At near vertical incidence, the strongest backscattering would occur with a perfectly flat surface or a gently undulating one. As the surface gets rougher, more of the vertically incident energy is scattered away from the radar look direction. Hence, the radar backscatter decreases with increasing wind speed and wave height near vertical, whereas it increases with increasing wind speed at angles beyond about $12°$. At near grazing incidence, the backscattering mechanism is dominated by non-Bragg scattering events, with backscattering cross-section of horizontal polarization exceeding that of vertical polarization of about 20-40 dB [13], [14]. This level of difference is much larger than that we expect from tilting modulation of Bragg roughness, and it can be better associated with steep wave features possibly going through wave-breaking process, with or without the generation of whitecaps. Portions of the wave, near grazing, may be partially obscured by waves between the radar and the wave being observed. Furthermore, both constructive and destructive interference may take place between the direct electromagnetic wave, striking the ocean, and the electromagnetic wave reflected off the surface. Shadowing and interference effects tend to cause a more rapid decrease in scattering coefficient with angle of incidence than predicted by Bragg scattering theory.

For ocean surfaces the absence of measurements causes large uncertainties in parameterizations of the wave height spectrum as a function of the frequency, the polarization, the incidence direction and the azimuthal look direction of the radar (e.g. [15]–[18]). Examples of such spectra are shown in Fig. 1; the high wavenumber end of the spectrum is the most sensitive to the wind. Note the huge variability between the four parameterizations depicted here, with the Apel spectrum showing much larger wind speed variability at Ka and W-band. Such variability in the wave spectrum lead to large uncertainties into the normalised backscattering cross sections as well. Similarly there is no characterization of normalised backscattering cross sections at moderate incidence angles for land surfaces.

This study aims at a detailed characterization of the polarimetric surface return (i,.e. σ_0^{VV}, σ_0^{HH}, σ_0^{VH}) both for water and

land surfaces to enable a proper design of W-scanning Doppler radars. Such characterization has been possible thanks to the recent upgrade of the National Research Council of Canada (NRC) airborne radar system (Sect. II). After describing the procedure for computing the normalised backscattering cross sections (Sect. III), in Sect. VI theoretical computations (Sect. IV) are thoroughly compared with measurements collected during an ESA field campaign described in Sect. V. Conclusions are drawn in Sect. VII.

II. THE NRC W-BAND AIRBORNE RADAR

The NRC Airborne W and X-bands Polarimetric Doppler Radar system (NAWX) was developed by the NRC Flight Research Lab in collaboration with ProSening Inc. for the NRC Convair-580 between 2005-2007. The NAWX antenna subsystem includes three W-band and three X-band antennas and a two-axis motorized reflector plate for one of the W-band antennas (Fig. 2). The NAWX radar electronics and data system is rack mounted inside the aircraft cabin while the antenna subsystem is housed inside an un-pressurized blister radome 137" × 28" × 25".

Three of the regular aircraft windows are replaced with metallic window plates fitted with customized bulkhead feed-through adaptors, for connecting the antenna ports from the W and X-bands RF units to the externally mounted antennas. Summaries of the NAWX system specifications are listed in Tab. I. The two radars have the following common features:

- two channel 12-bit digital receivers;
- electronic switching at both frequencies, allowing near-simultaneous sampling of the atmosphere in three planes along the flight-line using six antennas;

TABLE I: NRC Airborne W-band Radar Specifications.

RF output frequency	94.05 GHz
Peak transmit power	1.7 kW typical
Transmit polarization	H or V
Maximum Pulse Repetition Rate	20 kHz
Transmitter max. duty cycle	3 %
Pulse width	0.1-1 microseconds
Antenna ports (electronically selectable)	5
Receiver channels	2
Receiver polarization	Co and cross-polarization
Doppler	Pulse pair and FFT
Pulsing modes	Pulse pair and PDPP
Gaussian Optics Lens Antennas	1 x 12" single-polarization (nadir) 2 x 12" dual-polarization (side and aft)
Minimum detectable @ 1 km, 0.5μs pulse widths, 0.02 s dwell time]	-30 dBZ
A/D sample rate	70 MHz

- innovative design incorporating NRC-developed INS-GPS integrated navigation system for real-time Doppler correction;
- synchronized operation and data collection for dual-wavelength analysis;
- pulse pair and FFT Doppler processing.

The NAWX W-band has some unique components and design features that allow high resolution cloud measurements from an airborne platform as listed below:

- a space qualified W-band Extended Interaction Klystron (EIK) tube with 3% duty cycle, designed by CPI Canada for the CloudSat mission;
- a motorized two-axis reflector plate that allows the beam from the aft-looking dual-polarized 12" antenna to be reflected up to 40° in forward direction in either the horizontal or vertical (nadir) planes, providing dual-Doppler measurement in either horizontal and vertical (nadir) planes;
- dual channel DDS board (developed by ProSensing) is used to change the output frequency of each pulse for frequency hopping mode to de-correlate samples of the radar parameters and to generate standard pulses or linear FM chirp waveforms with selectable bandwidth and pulse length.

The NRC Airborne W-band and X-band Radar System (NAWX) has been used in several field campaigns (e.g., ISDAC, STAR and HAIC-HIWC [19]–[21]). The W-band system (NAW) was upgraded for this project to run in a polarization diversity pulse pair (PDPP) mode. For the NAW PDPP upgrade a conventional pulse-pair PP10 mode was modified (Fig. 3) allowing to collect conventional pulse pair and PDPP data from one of the two dual-polarization antennae. In this modified PDPP mode, sequences of H/V and V/H polarization diversity pulse-pairs are transmitted interleaved with staggered conventional H/H and V/V pulse-pairs. The main NAW upgraded features include the ability to transmit near double pulsing with short spacing as low as 5 μ s and recording the raw IQ radar data in PDPP mode.

The PDPP data is collected using either the dual-polarization aft-looking antenna and reflector combinations or the side dual-polarization antenna. Radar beam incidence angles ranging from 0° to 80° is achieved by performing different aircraft maneuvers (as listed in Tab. II) using the two

Fig. 3: NAW pulsing modes for the polarization diversity pulse pair (PDPP) configuration.

dual-polarization antennae and reflector (Fig. 2). The altitude of the aircraft during the maneuvers range from near 1.5 km to 7 km. The duration of each maneuver ranges from 1 minute (for a 45 degree orbit) to several minutes when performing roll sweeps. The aircraft stays at selected altitude for over 30 minutes while repeating the maneuvers and collecting PDPP data at four different PDPP pulse-spacing (6, 12, 20 and 40 μs).

Fig. 4: Geometry for a slant-looking radar (see text for details). Note that for the specific range here illustrated the surface is illuminated only by antenna sidelobes for the annulus shown. For longer ranges the integral in Eq. (3) over the annulus will include antenna main-lobe contributions.

TABLE II: NRC Airborne W-band Radar Flight Operation Modes.

Aircraft maneuver	Antenna	Description	Incidence angles
Horizontal transects	Aft + reflector	Different beam angles is achieved by by changing the reflector position while the aircraft maintains a constant altitude	0° to 46°
Orbits	Aft + reflector	Aft-looking beam is redirected to nadir view.	0° to 45°
	Aft + reflector	Change in aircraft roll angles from 0 to 45 degrees range.	
	Aft + reflector	Each orbit last 1-5 minutes depending on the roll angle selection	
	Side	Change in aircraft roll angles from 0 to 45 degrees	45° to 90°
Roll sweeps	Aft + reflector	Aft-looking beam is redirected to nadir view.	0° to 40°
	Aft + reflector	Change in aircraft roll angles from -40 to 40 degrees	

III. DERIVATION OF NRCS

Hereafter the procedure to compute the normalized backscattering cross section of the surface at different incident angles is briefly described.

A. Surface echo return shape

Fig. 4 shows the geometry for radar observations at slant angles, with a pulse hitting the surface at a given angle incidence angle, θ_{inc}. Here we assume that the radar transmitted pulse has a top hat shape with duration τ_p and is transmitted according to an antenna pattern characterised by a main lobe (light grey shaded cone) and different sidelobes (black envelopes). The power received at any time t (and corresponding range $r = ct/2$, where c is the speed of light) results from the contributions from targets located within the spheres centered at the radar and originated by the propagation of the pulse trailing and leading edges, depicted in Fig. 4 with orange and green lines, respectively. These targets comprise atmospheric scatterers (depicted in Fig. 4 as blue areas with the ones coloured in dark blue corresponding to the main antenna lobe) and the surface annular strip of terrain (shaded in yellow in Fig. 4) of inner radius

$$\rho_{in} = \sqrt{\left(\frac{c(t-\tau_p)}{2}\right)^2 - H_a^2} \quad (1)$$

and of outer radius:

$$\rho_{out} = \sqrt{\left(\frac{ct}{2}\right)^2 - H_a^2}. \quad (2)$$

Note that if the range of the trailing and the leading edge becomes shorter and remains larger than the aircraft height, H_a, the annular strip degenerates into a circle. The power received by the radar from the surface, P_r, assuming that the antenna gain is identical for transmission and reception, is given by an integration performed over the annular strip, S, [22], [23]:

$$P_r(r) = P_t \frac{\lambda^2}{(4\pi)^3} \int_S \frac{\sigma_0 \, G^2 \, |u(t-2r/c)|^2 \, e^{-2\int_0^r k_{att}ds}}{r^4} \, dS \quad (3)$$

where P_t is the transmitted power, λ is the wavelength of radar, G is the antenna gain, $u(t)$ is the complex voltage envelope of the transmitted pulse (for a top hat shape $|u(t)| = 1$ for $0 < t < \tau_p$), k_{att} is the attenuation coefficient, and where the normalised radar cross section ($NRCS$), σ_0, is defined as the surface radar backscatter cross section, σ_{surf}^{back} normalised to the surface area, A, and is expressed in dB units as:

$$\sigma_0[dB] \equiv 10\log_{10}\frac{\sigma_{surf}^{back}}{A}. \quad (4)$$

For a Gaussian pencil-beam circular antenna and for a homogeneous surface, Eq. (3) can be rewritten as ([11], [22] for details):

$$P_r(r) = \underbrace{P_t \frac{G_0^2\lambda^2\theta_{3dB}\phi_{3dB}}{2^{10}\pi^2\log(2)l_{tx}l_{rx}}}_{C} \frac{\sigma_0(\theta_{inc})}{r^2\cos(\theta_{inc})} \, e^{-2\int_0^r k_{att}ds} \, \mathcal{F}_{BF}(r)$$

$$(5)$$

where G_0 is the antenna gain along the boresight, θ_{3dB} and ϕ_{3dB} are the antenna 3 dB beamwidth in the horizontal and vertical, l_{tx} and l_{rx} are the loss between the antenna and receiver port and between the transmitter and the antenna port, respectively.

$\mathcal{F}_{BF}$ is a beam filling factor which is defined by comparing Eq. (5) and Eq. (3). A detailed expression and discussion of this term is provided by [22]. In general $\mathcal{F}_{BF}$ depends on the pulse duration, τ_p, on the range, r, on the specific observation geometry (H_a, θ_{inc}) and on the antenna illumination (via the antenna pattern).

For the Canadian Convair W-band radar a circular antenna pattern with θ_{3dB} equal to 0.76° can be assumed. The left panel of Fig. 5 depicts the normalised antenna two-way gain, G^2/G_0^2, in correspondence to surface points close to the boresight projection for a configuration when the aircraft is flying at 5 km altitude and the antenna is looking towards East at 60° incidence angle. Correspondingly the beam filling factor, $\mathcal{F}_{BF}$, is shown as a function of the range for two incidence angles (30° and 60°) with an airplane altitude of 5 km (right panel). The range is rescaled by r_S^{bs}, the surface range along the boresight direction (see magenta dotted line in Fig. 4). When $r - r_S^{bs}$ equals zero (red arrow in the right panel) the corresponding annular ring where the integration of Eq. (3) is performed, is plotted within the orange and green lines in the left panel. Note that for $\theta_{inc} = 60°$ the maximum of the beam filling factor is significantly lower than two, which is the result expected for low incidence angles since the surface return is much broader than at $\theta_{inc} = 30°$.

The surface return generally attains its maximum value when the center of the pulse intercepts the surface along the boresight (i.e. at $r = r_S^{bs} + c\tau_p/4$). The maximum of $\mathcal{F}_{BF}$ plotted as a function of different incidence angles and for different aircraft altitudes (Fig. 6) clearly shows the tendency
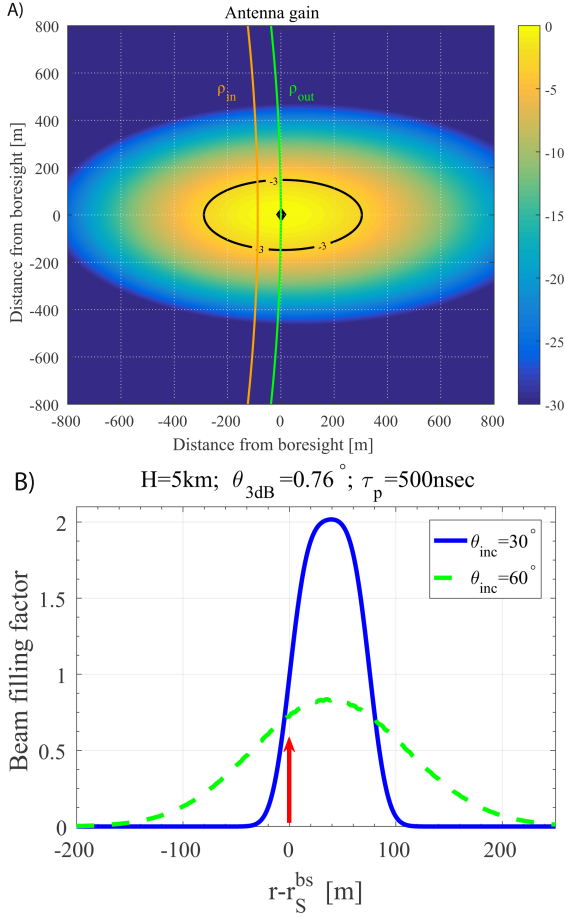
Fig. 5: Panel A: normalised antenna pattern at the ground for the Convair W-band radar flying at 5 km altitude and looking eastwards at 60 degree incidence angle. The coordinate system is centered around the boresight. The orange and green lines limit the annular ring for a range corresponding to the boresight range (indicated by the red arrow in the right panel) in correspondence to an incidence angle of 60°. Panel B: uniform beam filling factor as a function of range (rescaled by r_S^{bs}). Two incidence angles have been considered (30° and 60°) with corresponding surface ranges along the boresight direction equal to 5.77 and 10 km, respectively.

Fig. 6: Maximum of the beam filling factor, $\mathcal{F}_{BF}$, as a function of the Convair-580 W-band radar incidence angle. Different aircraft altitudes (as indicated in the legend) are examined. A Gaussian circular antenna with $\theta_{3dB} = \phi_{3dB} = 0.76°$ and a top hat pulse with duration $\tau_p = 500$ ns have been assumed.

B. Reflectivity calibration of radar channels

When the expression (5) is compared with the radar equation for atmospheric targets:

$$P_r(r) = \mathcal{C}_r \frac{|K_w|^2 Z_e}{r^2} e^{-2 \int_0^r k_{att} ds}$$

$$\mathcal{C}_r \equiv \frac{\pi^3}{2^{10} \log(2)} \frac{P_t \, G_0^2 \theta_{3dB} \phi_{3dB} c \tau_p}{l_{tx} l_{rx} \lambda^2} = C \frac{\pi^5}{\lambda^4} c \tau_p$$

with K_w being the dielectric factor of water at cm-wavelengths (assumed equal to 0.93) and C another radar constant, previously defined in Eq. (5). Eq. (5) can be rewritten as:

$$P_r(r) = \mathcal{C}_r \frac{|K_w|^2}{r^2} \underbrace{\frac{\lambda^4}{|K_w|^2 \pi^5} \frac{\sigma_0(\theta_{inc}) \, \mathcal{F}_{BF}(r)}{\cos(\theta_{inc}) \, c \, \tau_p}}_{Z_{surf}} e^{-2 \int_0^r k_{att} ds}$$

Note that, at vertical incidence, the maximum of the beam filling factor is 2 and the maximum surface return is obtained as:

$$
\begin{aligned}
Z_{surf} &= \frac{\lambda^4}{|K_w|^2 \pi^5} \frac{2\sigma_0(\theta_{inc}=0)}{c \, \tau_p} = \frac{\lambda^4}{|K_w|^2 \pi^5} \frac{\sigma_0(\theta_{inc}=0)}{\Delta r} \\
&= \frac{\lambda^4}{|K_w|^2 \pi^5} \frac{\sigma_{surf}^{back}(\theta_{inc}=0)}{A \Delta r}
\end{aligned}
\tag{6}
$$

which is the expected result with the last term on the right hand side representing the surface backscattering coefficient per radar backscattering volume (Δr is the radar radial resolution), corresponding to the analogous term when distributed targets are present.

By inverting Eq. (5), σ_0 can be derived but to this end the constant C has to be determined first, i.e. the radar must be calibrated. Note that, when considering different polarization

towards values significantly lower than two at moderate incidence angles, with a substantial reduction at high altitudes. The fact that the maximum of $\mathcal{F}_{BF}$ is not exactly 2 at small incidence angles is due to the change in range from the radar for the different portions which are significantly contributing to the integral (3), with the effect being exaggerated when the airplane is flying very low. On the other hand the range-integrated contribution of the surface is almost always the same in both cases (i.e. $\int_r \mathcal{F}_{BF} \approx c\tau_p$).

channels both in transmission (tx) and in reception (rx), we need to compute for each antenna four calibration constants:

$$C^{ij} \equiv C_{rx}^i C_{tx}^j = P_r^{ij}(r) \frac{r^2 \cos(\theta_{inc})}{\sigma_0^{ij} \mathcal{F}_{BF}(r)} e^{2 \int_0^r k_{att} ds}, \quad i,j = H, V \quad (7)$$

where P_r^{ij} is the power received in the $i-$channel when transmitting in the $j-$channel with a similar meaning of the notation for the quantities C^{ij} and σ_0^{ij}. Eq. (7) can be applied for instance at the range at which the surface return attains its maximum: in such case $r \approx r_S^{bs} + \tau_p/4$, the beam filling factor is provided by the values in Fig. 6 and the attenuation term is equal to $\exp[2\tau^{nadir}/\cos(\theta_{inc})]$ with τ^{nadir} being the optical thickness between the radar and the surface along the vertical direction (an horizontally homogeneous atmosphere is assumed to compute the corresponding optical thickness at slant angles).

Only relative values of the four unknowns of Eq. (7) are meaningful. Effectively there are only three unknowns. We can for instance assume C_{tx}^H to be equal to 1 so that C_{tx}^V will then represent the attenuation imbalance between the V and H transmission lines. From previous works ([11], [24]) it is known that at incident angle around 10 degrees, σ_0 over water surfaces is insensitive to wind speed, direction and polarization and is about 5 dB. We have exploited such calibration point for the ocean natural target to calibrate our radar system. By collecting all measurements close to $10°$ it is then possible to determine the quantities:

$$C^{VV} = C_{tx}^V[dB] + C_{rx}^V[dB] \equiv \alpha = [\text{calibrated value at } 10°] \quad (8)$$

and

$$C^{HH} = C_{rx}^H[dB] \equiv \beta = [\text{calibrated value at } 10°] \quad (9)$$

Eqs. (8-9) are two equations in three unknowns. An extra equation can be obtained by exploiting the fact that, thanks to the different pulsing modes of the Canadian Convair W-band radar (Tab. I), the linear depolarization at $H-$incidence of the surface (LDR_H^{surf}) can be measured in two different ways:

1) via pulse pair, by measuring at the time corresponding to the surface range the reflected power in both the co and cross-polar channels:

$$LDR_H^{PP} = \frac{P^{VH}}{P^{HH}} = \frac{C_{rx}^V C_{tx}^H}{C_{rx}^H C_{tx}^H} LDR_H^{surf} = \frac{C_{rx}^V}{C_{rx}^H} LDR_H^{surf}; \quad (10)$$

2) via PDPP, by measuring at the different times corresponding to the surface range the reflected powers in the co-polar channel for the first (H) and the second (V) pulses:

$$LDR_H^{PDPP} = \frac{P^{HV}}{P^{HH}} = \frac{C_{rx}^H C_{tx}^V}{C_{rx}^H C_{tx}^H} LDR_H^{surf} = \frac{C_{tx}^V}{C_{tx}^H} LDR_H^{surf} \quad (11)$$

By taking the ratio between Eq. (10) and Eq. (11) and expressing in dB units:

$$\underbrace{C_{tx}^V - C_{tx}^H}_{0} - C_{rx}^V + C_{rx}^H \equiv \delta = LDR_H^{PDPP} - LDR_H^{PP} \quad [\text{everywhere}] \quad (12)$$

with a similar expression holding for the LDR_V. If the system is properly cross-channel-calibrated then δ should be equal 0.

Alternatively, at nadir, the same LDRs are expected for the V and the H channels. Therefore the quantity:

$$2 C_{rx}^H - 2 C_{rx}^V \equiv 2\epsilon = LDR_V^{PP} - LDR_H^{PP} \quad [\text{close to nadir}] \quad (13)$$

should also be equal 0. Eqs. (8-9) and either Eq. (12) or Eq. (13) can be used to fully calibrate the calibration constants (e.g. $C_{tx}^V = \alpha - \beta + \epsilon$). Once the constants have been computed the powers are re-calibrated according to $P_{cal}^{ij} = P^{ij}/C^{ij}$; this ensures that the two channels are properly absolutely calibrated and internally cross-calibrated.

C. Antenna beam vector calibration

The accuracy in the calculation of the incidence angle is determined by the accuracy of the antenna beam pointing vector and the accuracy of the aircraft altitude and ground velocities measurements. The Convair-580 INS module and the NAWX W-band radar are co-located. This and the Convair INS-GPS real-time integrated data system provide precise altitude and velocity information. The beam pointing vectors are calibrated using data selected from many flights over stationary surface targets such as low-height vegetation farm lands. The calibration procedure is done using a similar optimization method described in [25]. For the side looking antenna, the antenna mount is rigid and no moving mechanism on the beam transmit path is involved, so the beam angle can be calibrated with a maximum root mean square error less than $0.1°$. The calibration of the beam vector of the aft antenna, however, would not be as accurate as that of the side antenna. This is because the aft antenna beam is re-directed via a reflector plate (Fig. 2) whose position is unknown. Thus, instead of optimizing for three parameters (elements of the beam vector of the aft antenna) we need to optimize for six parameters including the coordinates of the normal of the reflector. This is a complex optimization problem and therefore it is expected that the solution would not be stable. To overcome this problem, we assume that the normal of the reflector to be in the vertical plane and perfectly perpendicular to the aircraft fuselage at its home position. The position of the reflector then can be simply derived from elevation and azimuth angles provided by the two stepper motors. When the reflected beam vector from the aft antenna is estimated, the aft antenna beam vector can be calibrated. This procedure provides an error less than 0.5 deg in the estimation of the incidence angle when the aft antenna is used in PDPP mode. This implies up to 0.5 deg uncertainty in the incidence angle, which is acceptable for this radar cross section study.

IV. THEORETICAL COMPUTATIONS

We base the computation of the microwave scattering from a rough ocean surface, on the Small Slope Approximation (SSA) theory [26]. The small slope approximation does not invoke any arbitrary scale-dividing parameter separating small and large scale components of the roughness. The SSA can be applied to an arbitrary wavelength, provided that the tangent
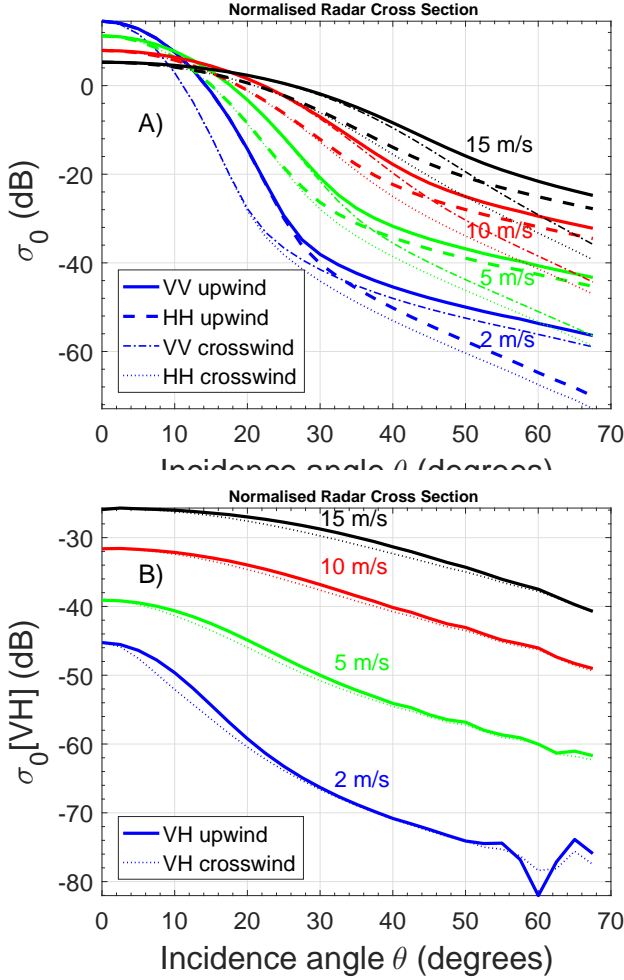
Fig. 7: Panel A): polarimetric normalized radar cross sections $\sigma_0[VV]$ and $\sigma_0[HH]$ at W-band for four wind speed cases (2, 5, 10 and 15 m/s) and two wind directions (upwind and crosswind) as indicated in the legend. Panel B): as in panel A) but for $\sigma_0[VH]$.

of grazing angles of incident/scattered radiation sufficiently exceeds the RMS slope of roughness. The slopes of sea-surfaces are generally small except for steep breaking waves which represent a relatively small percentage. The small slope approximation is adequate for the computation of scattering from both large (the Kirchhoff regime), intermediate and small scale (the Bragg regime) roughness. As this is the result of a regular expansion with respect to the power of the slope, the effect of higher-order corrections can be evaluated. In particular, we refer to the 2$^{\text{nd}}$ order approximation, named SSA2, which provides accurate estimates of the cross-polarized scattering components in the plane of incidence. The implementation of SSA2 is rather complicated as it requires the calculation of four-fold integrals with oscillating functions. This theoretical model has been largely validated against real measurements and empirical geophysical model functions at C and Ku-band (e.g. [27]–[29]). In Fig. 7 the SSA2 theory is combined with the spectrum proposed by [18] to estimate the polarimetric scattering signature of the ocean at W-band for four wind speed cases (2, 5, 10 and

15 m/s) and two wind directions (upwind and crosswind). Fig. 7 shows the variation of NRCSs as a function of the incidence angle for different wind speeds (different colors) and for different polarizations and wind directions (different line styles as indicated in the legend). Cross-polar scattering (panel B) is clearly less sensitive to the incidence angle than the co-polar scattering (panel A). For instance, in the case of 10 m/s up-wind, the NRCS in VH-polarization shows less than 15 dB dynamic range for incidence angles varying from $0°$ up to $65°$; this is a quite small number when compared to the 40-50 dB dynamic range of VV and HH-polarization. The behaviour of the cross-polar scattering with the wind direction looks different from the co-polar one (thick and thin lines correspond to upwind and crosswind conditions). Co-polar signals experience stronger modulation with the wind direction than the cross-polar signals: this is particularly evident at low incidence angles and low wind speeds. For a wind speed of 5 m/s, the peak-to-peak scattering modulation of VH-polarization, induced by the wind direction, is only 1 dB at $26°$ and 0.4 dB at $40°$: these are relatively small numbers when compared to the peak-to-peak modulation of VV and HH polarizations (of the order of 3-7 dB).

## V. THE ESA-FUNDED W-BAND AIRBORNE DEMONSTRATOR FIELD CAMPAIGN

In the framework of an ESA future mission activity, an airborne field campaign has been funded for characterizing the polarimetric backscattering cross sections of different surfaces in different conditions at incidence angles up to 60°. Four flights have been dedicated to surface characterization as listed in Tab. III. The NRC Convair-580 has been based at the NRC Flight Research Laboratory home base in Ottawa, Canada, except for the 13$^{\text{th}}$ May when a flight opportunity during a concurrent field experiment on the West Coast of Canada (Comox, BC) was exploited to fly over the Pacific ocean. The calibration procedure described in Sect. III-B has been performed on a case by case basis because of instabilities in the LNA of the system occurred during the field campaign. While Eqs. (8-9) can be used for the aft antenna, they cannot be used for the side antenna (for which it is not possible to achieve incidence angle lower than 45°). In such case we have used Eq. (12) to cross calibrate the two channels and we have used the overlapping region between 40 and 50 degrees to absolute calibrate the side antenna with the previously calibrated aft antenna.

A. Atmospheric gas correction

Atmospheric gases absorb strongly at W-band [11], [30], with the main contributions coming from oxygen and water vapour absorption but with the latter contributing to more than 90% of the total attenuation at temperature larger than $10°$ C and relative humidity above 50%. Because water vapor is mainly concentrated in the lower troposphere, surface measurements made from an airborne radar can be considerably attenuated especially when looking at slant angles. In this work the Liebe's absorption model [31] has been used but the 1780-GHz line is replaced by the continuum

TABLE III: List of flights with description of duration, location and targeted science.

Date	Location	Target	Flight duration
29/3/2016	Lake Ontario	Sea surface characterization	3.0 h
13/5/2016	Pacific ocean	Sea surface characterization	5.0h
30/5/2016	Ottawa and surroundings	Land surface characterization	3.5 h
1/6/2016	Lake Ontario	Sea surface characterization	3.5 h
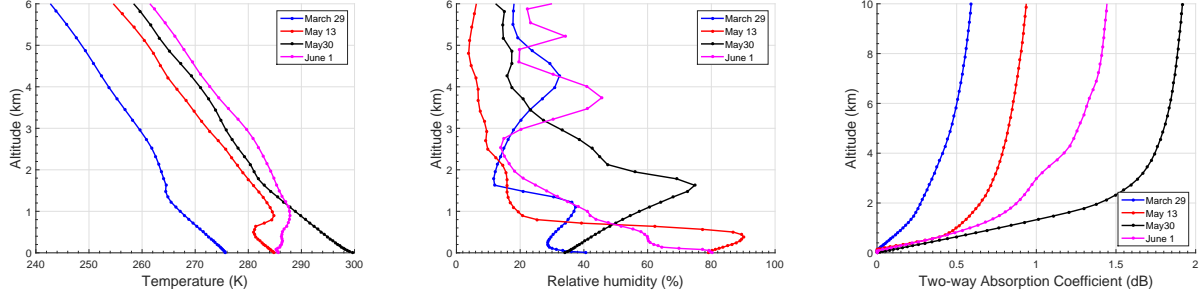
Fig. 8: Vertical profile of temperature (left panel), relative humidity (middle panel) and gas attenuation (right panel) for the flights of 29th March, 13th May, 30th May and 1st June 2016.

expression proposed by [32]. Recent findings by [33] show that such modelling properly represents the absorption of the water vapor continuum near 94 GHz.

Vertical profiles of gas attenuation coefficients are estimated from vertical profile of relative humidity, pressure and temperature provided by the European center for Medium-range Weather Forecast (ECMWF) reanalysis data with a resolution of $0.1°$ both in latitude and longitude for the cases of interest. The Fig. 8 reports the vertical profile of temperature, relative humidity and gas attenuation for the four cases listed in Table III.

The atmospheric conditions of the four days present marked difference both in terms of temperature and relative humidity. The surface temperature (Fig. 8, left panel) ranges from 275 K on the 29th March to 300 K on 30th May, while both 13th and 1st June registered surface temperatures around 285K. Lower values of ground relative humidity (Fig. 8, middle panel) were measured for 29th March and 30th May, while about double values (around 80%) were measured for the other two days. All days present different trends of the relative humidity with altitude with a tendency towards drier layers in the upper troposphere.

The high variability of the temperature and relative humidity profiles is mirrored in noticeable differences in the cumulative two-way gas attenuation for the four days. It ranges from values slightly larger than 0.5 dB for a path of 10 km of atmosphere for the coldest and driest day of 29th March to almost 2 dB for 30th May. Note that the maximum altitude at which the Convair aircraft can fly is about 6.5 km.

VI. RESULTS AND DISCUSSION

In this section, first some examples how data were collected are presented, then data are aggregated according to the surface type and analyzed distinctly so that the $NRCS$ and the LDR behaviours as a function of the incidence angle and the wind properties (for sea surfaces) can be identified.
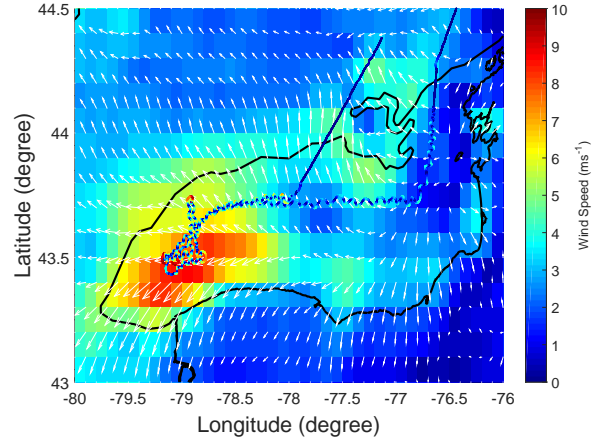

Fig. 9: Example of the 01/06/2016 flight pattern over Lake Ontario. The wind speed and direction at the surface are derived by the ECMWF high resolution reanalysis at 18 UTC. The wind intensity is color-coded while the wind direction is indicated by the white arrows. The black continuous lines mark the boundary between the lake and the land while the multi-coloured line corresponds to the airplane track color-coded according to the amplitude of the roll measured in degrees divided by a factor five.

A. Example of measurements

The 1st June flight pattern depicted as a multi-coloured line in Fig. 9 epitomizes the flight strategy pursued during all the flights listed in Tab. III. When entering the area of interest (in this case Lake Ontario, contoured with black lines) a gamut of observations at several different incidence angles have been gathered by changing the aircraft pitch and roll angles and the antenna port (aft or side). In Fig. 9 the color of the aircraft ground-track corresponds to the (absolute value) of the aircraft roll angle measured in degrees divided by 5. Roll angles up to $50°$ have been adopted, especially in the West region of the
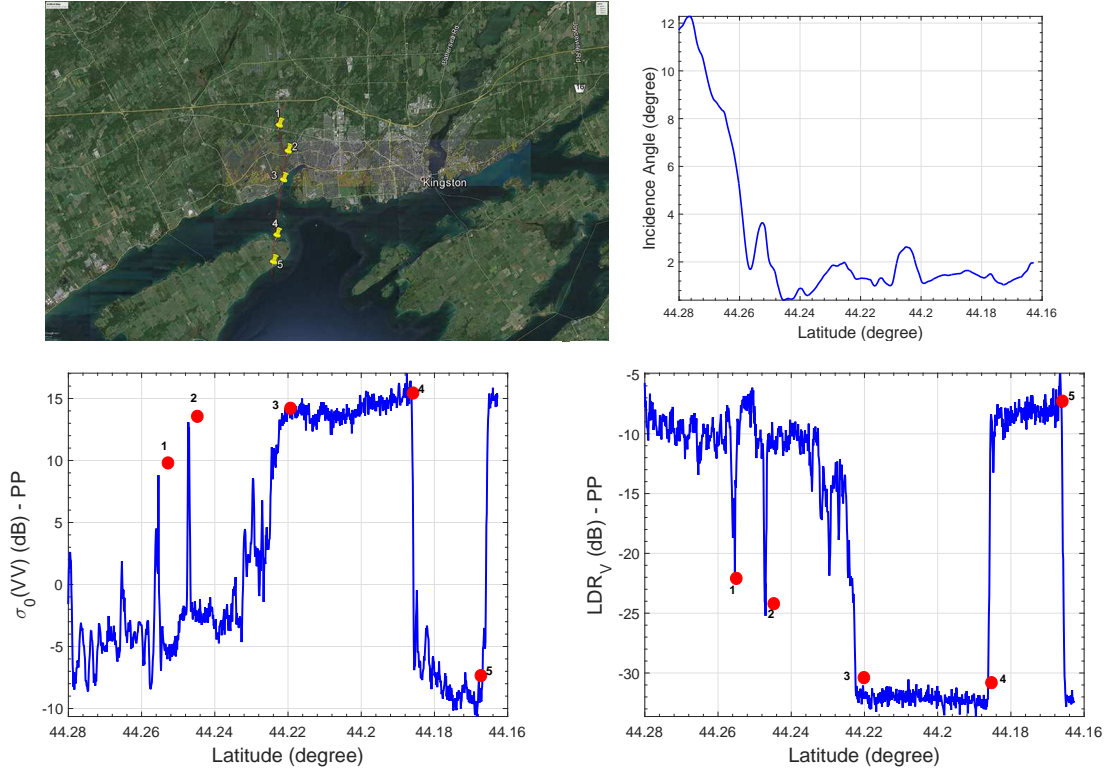
Fig. 10: Example of data collected during the 01/06/2016 flight over Lake Ontario.

lake where high winds up to 10 ms^{-1} were observed. In that region several circular orbits have been performed banking at an almost constant angle to assess the importance of the wind direction (relative to the antenna pointing direction) in affecting the NRCSs.

An example of a short leg from the 1st June 2016 flight is shown in Fig. 10 with the ground track first crossing Lake Ontario (placemark 3), then after a 4.5 km long stretch over the Lake passing over the Amherst island for a 2.3 km long transect before entering again the lake at placemark 5. The radar aft antenna was pointing mainly at nadir during this leg (top right panel). At such low incidence angles the lake surfaces clearly feature large σ_0 values and low LDR values (region between placemarks 3 and 4 and after placemark 5) with striking differences between water and land surfaces: the lake surface is much more homogeneous with a strong and weakly variable return (as already noted in Fig. 13, [11]). Viceversa land surfaces are generally characterized by highly variable and low NRCS and high LDR values. An exception is provided by asphalt roads and highways as highlighted by the placemarks 1 and 2. For the σ_0 this is in agreement with findings from [10] while for LDR this is expected with flat surfaces and rural/forested areas behaving like non depolarizing and strongly depolarizing surfaces, respectively.

A second example extracted from the 30th May 2016 flight over Ottawa city showcases the behave of the $NRCS$ at slant angles (Fig. 11). The projection of the antenna boresight at the ground is tracing roughly a semicircle embracing downtown Ottawa and crossing over the Ottawa river at the West end side of it. In this case the aft antenna is looking at the surface at incidence angles between 33° and 48° (top right panel). Because of the larger incidence angles the behaviour of the surface σ_0 is now different from the previous case, with water surfaces being much weaker targets than land surfaces. This is highlighted in the bottom left panel when considering the times of the overpasses over the four water bodies around 18:04:45, 18:05:02, 18:05:12 and at the very end of the recording period, and the corresponding drop in the NRCS values. LDR values for land surfaces exhibit a behaviour similar to that at small incidence angles with LDR values in the range between -10 and -5 dB; viceversa over water LDR is again small and tend to drive the cross polar signal below the minimum detection threshold.

B. Results for water surfaces

By using the aircraft geolocation and the antenna pointing direction the position of the antenna boresight at the ground is computed every 0.5 s. Only cases confidently over water (boresight in water within 1 km) are retained for further analysis.

The wind speed and direction at the surface are derived by the closest ECMWF high resolution reanalysis. All available environmental and buoys station data from both the US and Canadian stations Lake Ontario show a very good agreement with the ECMWF reanalysis products (which are likely to assimilate most of these buoys). This makes possible to analyze the dependence of the NRCS and LDR on the incidence angles is analyzed, as well as the NRCS dependence on the wind speed and direction.
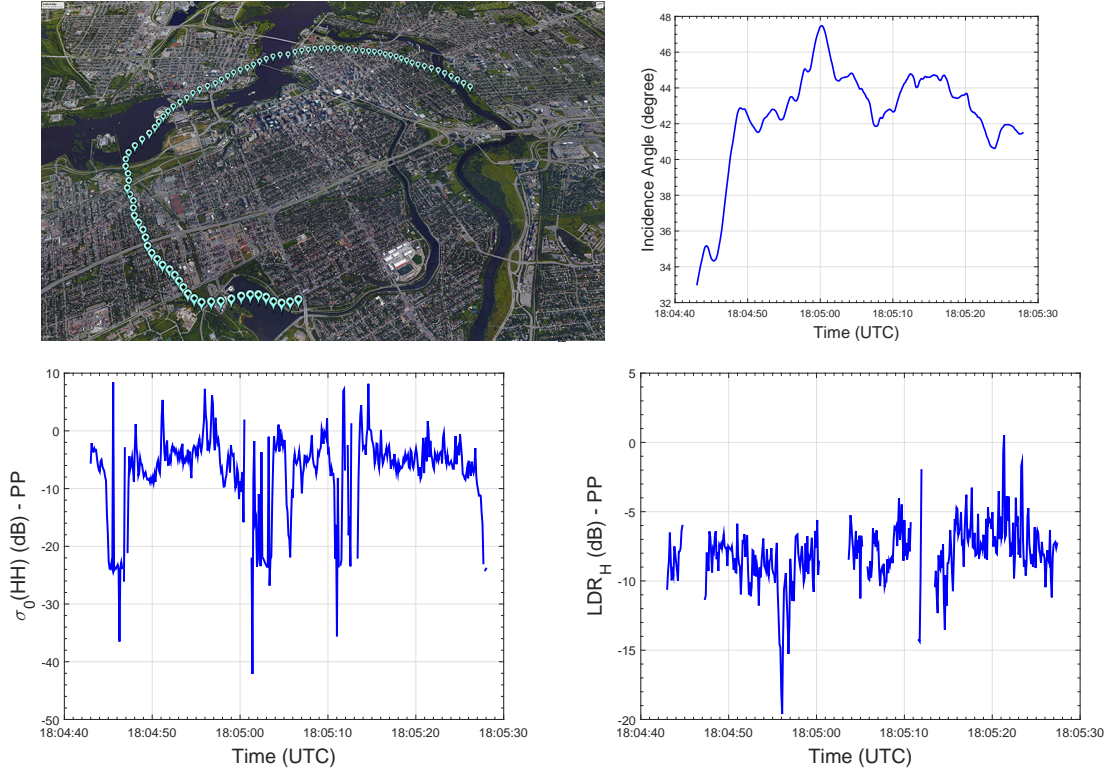
Fig. 11: Example of data collected during the 30/05/2016 flight over Ottawa city.

1) NRCS wind speed dependence: The wind speed during the three different flights ranged between less than 2 ms^{-1} to about 10 ms^{-1}. Panel A) in Fig. 12 describes the trend of σ_0^{HH} for different wind speed intervals, 2 ms^{-1} wide, reporting the median and the 10th and the 90th percentile for $2°$ incidence angle bin. As expected the NRCSs are monotonically decreasing with incidence angles. The behaviour below $20°$ incidence angles is in very good agreement with previous measurements, [34]. At near-nadir incidence angles and with very low winds (and corresponding to almost flat surfaces), the water surfaces act like a perfect mirror strongly backscattering the incident radiation with σ_0 values sometimes exceeding 20 dB. When increasing the wind speed and the surface roughness accordingly, NRCSs tend to decrease down to 8 dB at quasi-nadir angles.

At about $10°$, as previously noted there is a cross-over point, with cross sections only slightly changing with wind intensities. At larger incidence angles stronger winds tend to produce larger σ_0, again in agreement with theory. The observed data are well centered within the expected theoretical envelope range -with the solid blue and red line limiting the shading grey area indicating the theoretical σ_0 estimated for wind speed of 5 and 15 ms^{-1}, respectively, typically showing substantially lower variability. At incidence angles larger than $35°$, the decrease of σ_0 with incidence angle seems to slow down with σ_0 values within the [-20:-35] dB range for incidence angles between 40 and $50°$. This reduction in the rate of decrease in the NRCS with incidence angle is not mirrored in theoretical results (Panel A in Fig. 7). In the V-channel results are very similar to the H-channel (Panel B).

The differences predicted by theory (Panel A in Fig. 7) are not observed. The verification of this property requires more attention in future observations.

2) NRCS wind direction dependence: not only the wind speed but also the relative direction between the radar antenna beam-pointing vector and the wind affects the σ_0. From a theoretical point of view, if the radar antenna beam-pointing vector is orthogonal to the wave motion (cross-wind) smaller values of σ_0 are expected compared to when the radar antenna beam-pointing vector is parallel to the wind/waves. For the latter condition higher values are predicted for up-wind conditions.

During the 1st June flight a number of orbits at different incidence angles, ranging mainly between $30°$ and $70°$, allowed both cross- and up/down-wind measurements of σ_0. Fig. 13 shows the median σ_0 for $10°$ intervals of relative direction between the radar antenna beam-pointing vector and the wind and for $5°$ intervals of incidence angle.

The measured σ_0 presents two maxima around $0°/360°$ (down-wind) and $180°$ (up-wind) regardless the incidence angle, with higher values for the latter; two minima are found around $90°$ and $270°$ (cross-wind) in agreement with theoretical predictions. Fig. 13 also shows that lower σ_0 values correspond to larger incidence angles as previously discussed. A more detailed analysis of a single orbit (Fig. 14) clearly demonstrates the previous result with maxima around $0°/360°$ and $180°$ as well as the minima around $90°$ and $270°$. The maximum around $0°$ presents also a marked dependence on the incidence angles, with higher σ_0 values at lower incidence angle values. Note that the peak to trough variability exceeds 15 dB. This wind direction variability
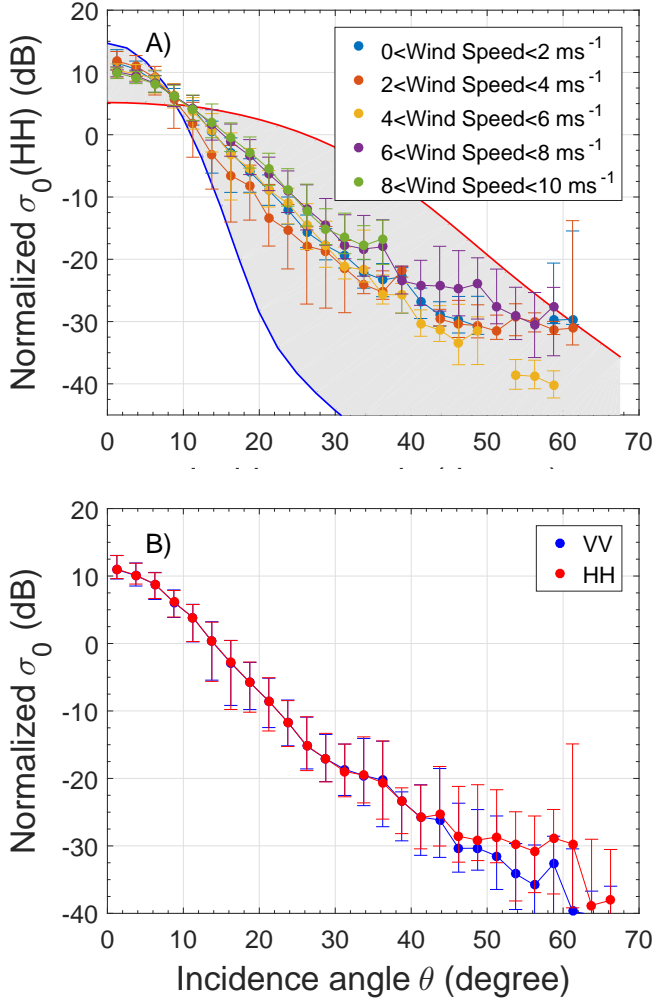
Fig. 12: Panel A): measured σ_0^{HH} over water surfaces as function of incidence angles for different wind speed classes as indicated in the legend. The dots indicate the median, while the bars the 10th and the 90th percentile for 2° incidence angle bin. The solid blue and red line limiting the shading grey area indicate the theoretical σ_0 estimated for wind speed of 5 and 15 ms^{-1}, respectively. Panel B): comparison between σ_0^{HH} and σ_0^{VV} as a function of the incidence angle.

Fig. 13: Median σ_0 over water surfaces as function of the relative direction between the radar antenna beam-pointing vector and the wind. Results have been clustered according to five-degree-wide incidence angle classes (as indicated in the legend).

Fig. 14: Measured σ_0 over water surfaces as function of relative direction between the radar antenna beam-pointing vector and the wind for the flight of the 16:26:40 UTC.

seems to be quite strong and is an important finding of our measurements. A similar but slightly weaker dependence (9 dB peak to through) was already documented by [11] at $\theta_{inc} \approx 29°$ (see their Fig. 12).

C. LDR measurements

Fig. 15 shows the LDR trend for both polarization over water surfaces as function of the incidence angle for 5° incidence angles bin: circles correspond to the median while the error-bars are associated to 10th and the 90th percentile. Note that, because of reciprocal behaviour i.e. $\sigma_0[VH] = \sigma_0[HV]$, any difference between LDR_V and LDR_H is due to differences in the co-pol cross sections. The LDR is pretty constant for incidence angle lower than 20°: this is attributed to a saturation effect induced by the cross isolation of the radar, which is
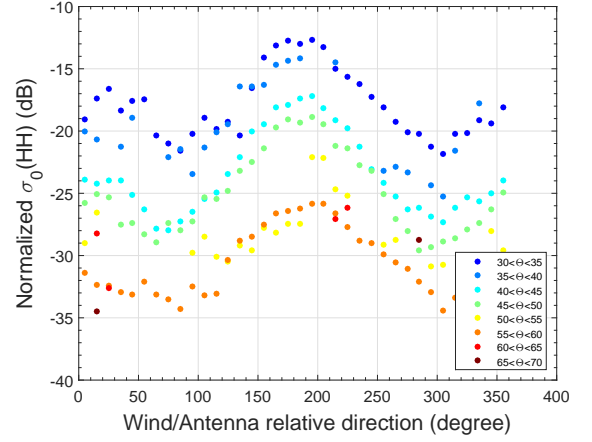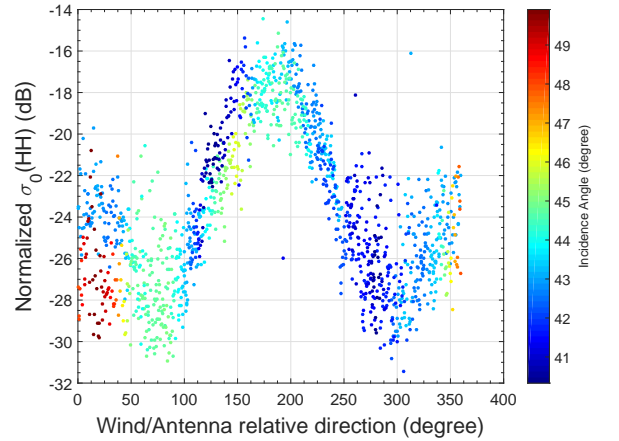
estimated to be circa -34 dB. The theoretical computations show indeed much smaller values for incidence angles below 20° especially with weak winds. At larger incidence angles experimental results seem to be more in line with theoretical predictions, with an increase in LDR up to close to -10 dB at 70° incidence angle.

D. Results for land surfaces

The flight of 30th May 2016 was entirely dedicated to characterize the land surface radar return. The flight was conducted around Ottawa city (in the following labelled as "urban") and over different land types: one dominated by crops and patches of forest South of Ottawa ("rural") and one covered by forests ("forest"). As for the other analyzed flights, a number of legs with different roll inclinations were alternated to orbits at a roughly constant incidence angle. The
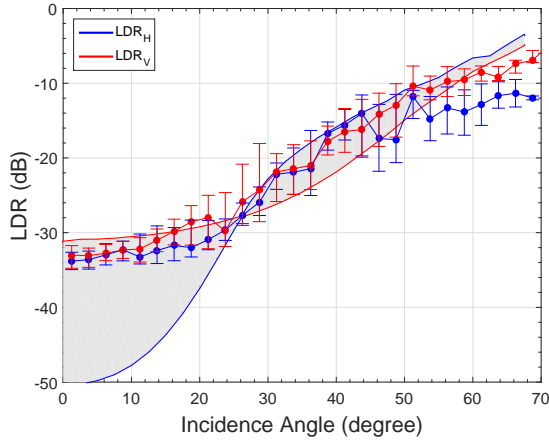
Fig. 15: Measured LDR as function of the incidence angle for water surfaces. Measured median and 10th and 90th percentile as function of incidence angle for water surface. The solid blue and red line limiting the shading grey area indicate the theoretical LDR estimated for wind speed of 5 and 15 ms^{-1}, respectively.
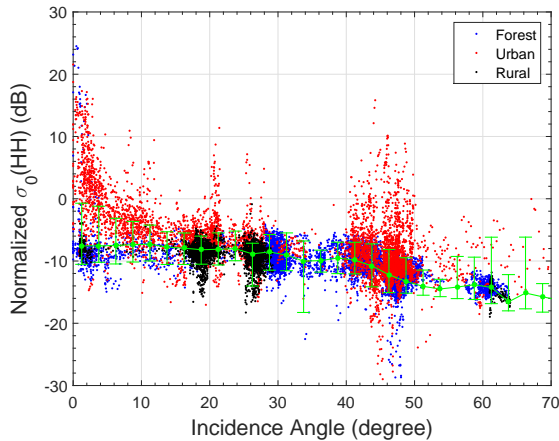

Fig. 16: The measured σ_0 for different surfaces as function of the incidence angle for the flight of 30th May 2016 (land surfaces only). Blue, red and black dots correspond to forest, rural and urban surfaces, respectively.

Fig. 16 shows the measured σ_0 as function of the incidence angle at both H- and V-polarization.

Compared to the results over water, the σ_0 over land surfaces is generally constant regardless the incidence angle, slightly decreasing for larger values of the incidence angles. Both forest (blue dots) and rural (black dots) surfaces present very similar results, whilst urban surfaces (red dots) generate slightly higher values of σ_0 and are also characterized by a more marked spread of σ_0. The higher values at small incidence angles are certainly related to the presence of several stretches of water (see previous Fig. 11) and of flat roads and buildings. Very high values of σ_0 are also obtained for incidence angles clustered mainly around 25° and 45°, with the outliers probably associated to strong

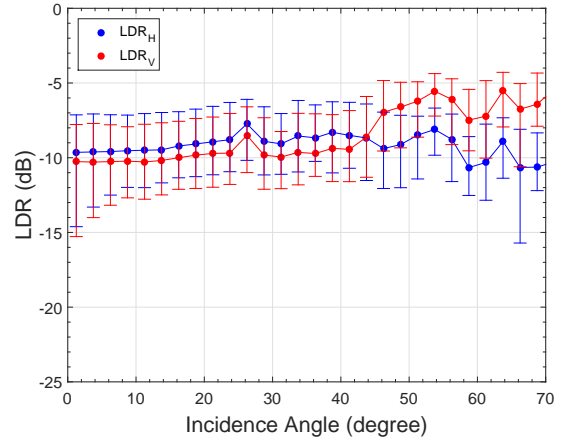reflection from buildings. Fig. 17 shows a slight increase of

Fig. 17: Measured median and 10th and 90th percentile of LDRs as function of incidence angle for land surfaces.

the LDR increasing with the incidence angle. The spread is generally constant regardless the incidence angle except for larger angles where the sample size measurements is lower. The difference between H- and V-polarization LDRs is less marked than for water.

VII. CONCLUSIONS

The understanding of W-band radar surface backscattering properties at moderate viewing angles is crucial for the design of future space-borne missions deploying scanning W-band radars. This study presents the results of a recent campaign conducted over the Great Lakes Region focused at characterizing the W-band normalized backscattered cross sections (σ_0) for V and H polarization and the Linear Depolarization Ratios (LDR_V and LDR_H) for land and sea surfaces. For *sea-surfaces* key results can be summarized as following:

1) While the observed σ_0 agrees with previous reports at small incidence angles, a strong decrease with increasing incidence angles occurs between 20° and 50° (e.g. at 50° incidence angle the surface is typically 40 dB less reflective than at nadir). This is as predicted by theoretical models and as observed at lower frequencies. In disagreement with theoretical predictions the rate of decrease of measured σ_0s seem to reduce at incidence angles above 40°-50°.

2) There is a strong dependence of normalized backscattered cross sections both on the wind speed (with recorded values up to 10 m/s in this work) and on the wind direction, with larger values found in presence of higher wind speeds and when the radar antenna is looking up-wind. Minima in backscattered cross sections are observed when looking cross-wind.

3) Contrary to theory the observations do not show a significant polarization dependence (i.e. any difference between σ_0^{HH} and σ_0^{VV}).

4) The linear depolarization ratios are steadily increasing from values certainly lower than -30 dB, at vertical

incidence, to values of about -10 dB at incidence angles of about 60°-70°, with a good matching between observations and theoretical predictions.

In contrast, both backscattering cross sections and linear depolarization ratios of *land surfaces* are not characterised by a strong angular dependence. σ_0 and LDR values typically range between -20 and 0 dB and between -15 and -5 dB, respectively. Close to nadir backscattering can reach very high values, especially over urban areas where flat man-made surfaces can strongly enhance specular reflection.

Acknowledgment

Leo Pio D'Adderio Leo Pio D'Adderio graduated at the University of Ferrara, Italy, with a thesis in Cloud Microphysics and Precipitation, and received the Ph.D. degree in Physics at the same University. He is experienced in microphysical, spatial and temporal properties of the drop size distribution, experimental research in ground-based radars, in scattering computations by ice particle populations. Currently, he has a post-doc position at the University of Ferrara, Department of Physics and Earth Science and he is visiting scientist at NASA-GSFC.

Cuong Nguyen Cuong Nguyen received the B.E. degree in electronics and telecommunications from Hanoi University of Science and Technology, the M.S. and the Ph.D. degrees in electrical and computer engineering from Colorado State University, Fort Collins. He is currently with the Flight Research Laboratory, National Research Council of Canada. His research interests include radar signal processing, development of retrieval algorithms for cloud and weather radars, modeling and simulation of radar systems, and radar data quality control.

Alessandro Battaglia Alessandro Battaglia, graduated at the University of Padova, Italy, with a thesis in Particle Physics and received the Ph.D. degree in Physics at the University of Ferrara, Italy. He is experienced in cloud and precipitation microwave remote sensing and radiative transfer. His research interests include development of retrieval algorithms, modeling and simulation of radar systems for future space missions. Currently, he is Associate Professor at the University of Leicester, Department of Physics and Astronomy and Member of the NASA Precipitation Measuring Mission Science Team.

Franco Fois Dr. Franco Fois received the Master degree in electronics engineering from the University of Rome La Sapienza in 2003. From 2003 to 2008, he worked in Alenia Spazio as a microwave instrument engineer with focus on radar sounders and synthetic aperture radars. He has been involved, as a performance engineer, in the preparation of several Earth Observation Missions such as MetOp-SG Scatterometer, Biomass, CoreH2O, Saocom-CS and Sentinel1-CS. In 2015, he received the PhD degree from the Delft University of Technology with emphasis on Ocean Scatterometry, sea surface scattering theories and microwave sea surface Doppler signatures. In January 2016, he joined Airbus Defence and Space, as a System Engineer and Scientist carrying out a number of studies on future Earth observation missions.

Mengistu Wolde Mengistu Wolde received a B. Sc. Degree in physics from Addis Ababa University and an M.Sc. and PhD degrees in Atmospheric Science from the University of Wyoming. He joined the Flight Research Laboratory of the Canadian National Research Council (NRC) in 2000. He has extensive experience in initiating and leading aircraft based in-situ and remote sensing projects in support of diverse research applications in atmospheric science, aircraft icing, satellite CAL/VAL and radar meteorology. He was the PI for the development of the NRC Airborne W and X-band Radar (NAWX). Currently, he is a Senior Research Officer and also manages the NRC Convair-580 Research Aircraft and the Convair Research Team.

Anthony Illingworth Prof. Anthony Illingworth joined the Department of Meteorology at Reading in 1993. For over 30 years he has worked with the large 25 m radar antenna at Chilbolton, Hampshire developing methods for improved estimates of rainfall. Since 2000 he has also been involved in the development of spaceborne missions for observing cloud properties on a global scale. He is the lead European scientist on the EarthCARE mission, a joint European/Japanese satellite due to be launched in 2018. The Doppler radar and advanced lidar on this satellite will provide global profiles of clouds, aerosol, precipitation and radiation to better understand the earth's radiation balance and improve weather forecasts.

Rolv Midthassel Rolv Midthassel, graduated at the University of Glasgow with a European Master of Engineering in Electronics Engineering with Optoelectronics in 1995. He spent several years in industry working on radar developments at Ericsson Radar, Norway and on satellite communication terminal developments for the Norwegian company NERA, with focus on Microwave Engineering. He joined the European Space Agency in 2001 and after many years in the Telecommunication Directorate, he is currently working as an Instrument Engineer in the Future Instrument Division of the Earth Observation Directorate.